

## Article

# Asymmetry of Structural and Electrophysical Properties of Symmetrical Titania Nanotubes as a Result of Modification with Barium Titanate

Elizaveta Konstantinova <sup>1,\*</sup>, Vladimir Zaitsev <sup>1</sup>, Ekaterina Kytina <sup>1</sup>, Mikhail Martyshov <sup>1</sup>, Timofey Savchuk <sup>1,2</sup>, Danil Butmanov <sup>1,2</sup>, Daria Dronova <sup>2</sup>, Daria Krupanova <sup>2,3</sup>, Lidiya Volkova <sup>2,4</sup> and Andrey Tarasov <sup>2</sup>

- <sup>1</sup> Physics Department, M.V. Lomonosov Moscow State University, Moscow 119991, Russia; vzaitsev@phys.msu.ru (V.Z.); kytina.ev19@physics.msu.ru (E.K.); martyshov@physics.msu.ru (M.M.); u122155@edu.miet.ru (T.S.); 8191252@edu.miet.ru (D.B.)
- <sup>2</sup> Institute of Advanced Materials and Technologies, National Research University of Electronic Technology–MIET, Moscow 125993, Russia; u102039@edu.miet.ru (D.D.); krupanova.da@phystech.edu (D.K.); 8210079@edu.miet.ru (L.V.); u123168@edu.miet.ru (A.T.)
- <sup>3</sup> Phystech School of Electronics, Photonics and Molecular Physics, Moscow Institute of Physics and Technology (National Research University), Moscow 141701, Russia
- <sup>4</sup> Department of Structural Analysis and Metrology, INME RAS, Leninsky Prospekt, Moscow 119991, Russia
- \* Correspondence: konstantinova@physics.msu.ru

**Abstract:** Anodic titania nanotubes (TiO<sub>2</sub>-NT) are very promising for use in photocatalysis and photovoltaics due to their developed surface, symmetrical structure and conductive properties, which, moreover, makes them a convenient matrix for creating various nanocomposites. Herein we propose a new facile way of synthesizing symmetrical TiO<sub>2</sub>-NT followed by a modification with barium titanate (BaTiO<sub>3</sub>) nanoparticles, combining the advantages of electrochemical oxidation and hydrothermal synthesis. The electrophysical and optoelectronic properties of the formed nanocomposites have been studied. An asymmetry of the current–voltage characteristics was revealed. It is shown that during the barium titanate deposition, a symmetry-breaking nanoheterojunction TiO<sub>2</sub>/BaTiO<sub>3</sub> is formed. Using EPR spectroscopy, paramagnetic defects (titanium, barium and oxygen vacancies) in the samples were determined. It was observed for the first time that upon illumination of titania nanotubes modified with BaTiO<sub>3</sub>, the asymmetrical separation of photoexcited charge carriers (electrons and holes) between TiO<sub>2</sub>-NT and BaTiO<sub>3</sub> occurs, followed by the capture of electrons and holes by defects. As a result, the photoinduced charge accumulates on the defects.

**Keywords:** symmetrical titania nanotubes; TiO<sub>2</sub>/BaTiO<sub>3</sub> nanoheterojunction; asymmetrical current–voltage characteristics; charge accumulation; EPR



**Citation:** Konstantinova, E.; Zaitsev, V.; Kytina, E.; Martyshov, M.; Savchuk, T.; Butmanov, D.; Dronova, D.; Krupanova, D.; Volkova, L.; Tarasov, A. Asymmetry of Structural and Electrophysical Properties of Symmetrical Titania Nanotubes as a Result of Modification with Barium Titanate. *Symmetry* **2023**, *15*, 2141. <https://doi.org/10.3390/sym15122141>

Academic Editor: György Keglevich

Received: 10 October 2023

Revised: 19 November 2023

Accepted: 24 November 2023

Published: 1 December 2023



**Copyright:** © 2023 by the authors. Licensee MDPI, Basel, Switzerland. This article is an open access article distributed under the terms and conditions of the Creative Commons Attribution (CC BY) license (<https://creativecommons.org/licenses/by/4.0/>).

## 1. Introduction

Currently, one of the most important tasks of humanity is to develop rational methods for using underutilized energy sources [1]. The implementation of flexible piezoelectric generators makes it possible to create wearable electronics, including medical devices that do not require frequent recharging [2–7]. The usage of solar energy can reduce the consumption of fossil hydrocarbons by generating electricity, obtaining hydrogen from water and converting atmospheric carbon dioxide into light hydrocarbons. Additionally, using sunlight to purify water can increase the quantity and purity of drinking water around the world.

For a long time, titania (TiO<sub>2</sub>) has remained the object of intensive scientific research devoted to the development of new methods for the synthesis of the material in various structural forms, including monophasic structures and nanostructures, as well as nanocomposites [8–12]. The attractiveness of nanostructured TiO<sub>2</sub> for researchers in recent decades

is due to its significant specific surface area [8–12]. The wide and varied range of applications of nanocrystalline  $\text{TiO}_2$  includes use in solar cells, in gas sensors, as a photoanode for photoinduced water decomposition, in the food and pharmaceutical industries, in optoelectronics and memristors due to its chemical resistance, suitable band edge potentials and propensity to form oxygen vacancies in its structure [8–12]. It is used for the photocatalytic purification of air and water, as well as for the photocatalytic conversion of carbon dioxide into more complex carbon compounds and other energy-intensive processes [9,12–14]. Researchers were able to compensate for the major drawback of  $\text{TiO}_2$ 's wide bandgap and ultraviolet light requirement by introducing impurities and/or defects into its structure [12–17]. Impurity centers successfully “reduce” the band gap of  $\text{TiO}_2$  by locating energy levels inside it and providing photon absorption using these energy levels [12,14–18].

Symmetrical titania nanotube arrays ( $\text{TiO}_2$ -NT) are a promising nanomaterial with potential applications in photocatalysis and photovoltaics [8,12,13].  $\text{TiO}_2$ -NT arrays are used in solar cells and wastewater treatment due to their huge specific surface area and conductive properties, which also make them a convenient matrix for creating various nanostructures [8,12]. In [14–17], the authors investigate ways to control the concentration and type of paramagnetic centers in titanium oxide nanostructures in order to control their photocatalytic and optic properties. Modification of the surface and composition of  $\text{TiO}_2$  nanostructures of various morphologies (nanotubes, nanoparticles, nanorods) in order to control its optical and electronic properties remains a relevant topic [18–22]. For example,  $\text{BaTiO}_3$  nanoparticles, which have beneficial properties, can be one of the promising modifiers.  $\text{BaTiO}_3$  nanoparticles have the potential for numerous applications in various fields such as electronics, catalysis, biomedicine, electromechanical generators and optics [2–6]. In biomedicine,  $\text{BaTiO}_3$  nanoparticles have the potential for targeted drug delivery and cancer treatment [4]. They can also generate electricity from mechanical vibrations and movements and are used in optics for optical switching [6]. Nanostructured barium titanate has a high dielectric constant and piezoelectric and ferroelectric properties, making it useful for capacitors, sensors and energy storage devices in electronics [2–6]. In addition,  $\text{BaTiO}_3$  nanoparticles are used in catalysis for reactions such as photocatalytic degradation of organic pollutants and hydrogenation.

Combining symmetrical titania nanotubes with  $\text{BaTiO}_3$  nanoparticles will make it possible to obtain a material with new unique properties for use in various fields of science and technology. The formed heterojunction should contribute to the spatial separation of charge carriers, potentially expanding the possibilities of application of devices based on such composites in photovoltaics [3], photocatalysis [2,21–23] and piezoelectric current sources [5]. At the same time, only a few works have aimed at investigating the nature of paramagnetic centers (defects) in such structures and their relation to the electronic properties of heterostructures.  $\text{BaTiO}_3$ - $\text{TiO}_2$  heterostructures can be synthesized using symmetrical arrays as a matrix, through a simple hydrothermal process with barium hydroxide. This approach will allow the formation of porous heterostructure immobilized on a conducting substrate, which is required for most applications, but the synthesis parameters need to be discovered. It should be noted that before the deposition of barium titanate, the pores in titanium dioxide are located strictly vertically and parallel to each other, forming a symmetrical system of pores. Decoration with  $\text{BaTiO}_3$  nanoparticles breaks this symmetry, which leads to pore asymmetry; since  $\text{BaTiO}_3$  nanoparticles fill the vertical pores of titania, the pores between the  $\text{BaTiO}_3$  nanoparticles are arranged randomly. The preparation and comparative analysis of the structure, composition, electrical properties, type and properties of defects of the original samples ( $\text{TiO}_2$ -NT) and samples with  $\text{BaTiO}_3$  nanoparticles deposited on the surface of titania is a new original study that reveals the influence of the asymmetry of the structural properties of  $\text{TiO}_2$ -NT/ $\text{BaTiO}_3$  nanocomposites on their electrical properties and defect characteristics.

## 2. Materials and Methods

### 2.1. Nanotube Arrays

Samples of anodic titanium oxide nanotube arrays were obtained by electrochemical oxidation of titanium foil in potentiostatic mode (60 V) in two stages. The first stage of anodic oxidation was carried out to form a sacrificial layer of the TiO<sub>2</sub>-NT array for 30 min. The sacrificial layer was removed by cathodic polarization in a sulfuric acid solution. This step is necessary to increase the uniformity of the future array obtained in the second stage. The second stage lasted 60 min. After formation, the samples were washed in ethanol. The composition of the electrolyte used per 100 mL was 0.3 g NH<sub>4</sub>F, ethylene glycol, and 2 mL of deionized water (18.2 MOhm·cm). The cathode was a 2 × 2 cm platinum grid. The current source was AKIP-1125 (Prist, Moscow, Russia).

After formation, the TiO<sub>2</sub>-NT arrays were subjected to heat treatment in an Averon EMP 11.1 muffle furnace (Averon, Yekaterinburg, Russia) in air at 450 °C for 1 h for crystallization.

### 2.2. Surface Modification

The modification of the obtained samples of TiO<sub>2</sub>-NT arrays was carried out by hydrothermal treatment in a 0.1 M aqueous solution of Ba(OH)<sub>2</sub>. For this purpose, a steel autoclave with a fluoroplastic liner was used. The treatment was carried out in a muffle furnace at a temperature of 210 °C for various times (3, 6 and 9 h). After the autoclave cooled, the samples were removed and washed in deionized water.

The main stages of the sample synthesis process are shown in the in the following diagram (Figure 1):

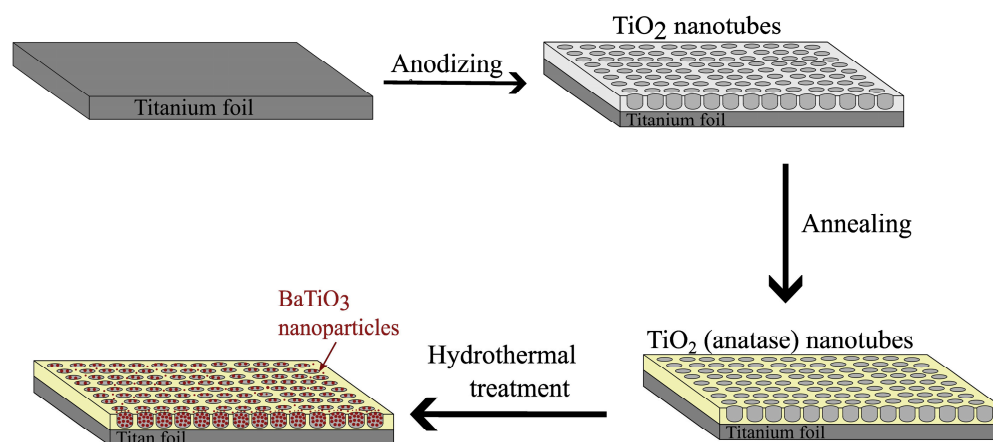


**Figure 1.** Main stages of the sample synthesis process.

### 2.3. SEM, EDX, XRD

The morphology of the surface of the samples was studied using a Helios G4C X dual-beam scanning electron microscope. Recording mode: accelerating voltage, 5 kV; current, 21 pA; shooting was carried out at angles of 0 and 52 degrees in the TLD (Through the Lens Detector) secondary electron mode. The X-ray diffractometer Rigaku MiniFlex XRD was used to analyze the obtained samples. CuK $\alpha$  radiation 1.54 Å.

### 2.4. Optics

Raman spectra were recorded using a SOL Instruments Confotec NR500 spectrophotometer (Minsk, Belarus), equipped with a Peltier element for cooling and a diode laser with a wavelength of 532 nm. Diffuse light-scattering spectra from the obtained samples were recorded using an LS-55 Perkin Elmer spectrometer operating in the spectral range of 200–800 nm with a spectral slit width from 2.5 to 20 nm. The design features of the spectrometer and control software make it possible to record spectra of diffuse reflection of light at different angles of incidence of the probing beam on the surface.

### 2.5. Electrophysics

To study the electrical properties of the samples, capacitor-type structures were used, in which a layer of TiO<sub>2</sub> nanotubes modified with barium titanate was located between two metal electrodes. The bottom electrode was a titanium substrate on which symmetrical nanotube samples were directly formed. The upper electrode with a size of 3 × 4 mm<sup>2</sup> was also made of the substrate material and was tightly pressed from above to a layer of nanotubes coated with barium titanate. Current–voltage characteristics of the samples were obtained using a Keithley 6487 picoammeter. Voltage was applied to the sample from a source built into the picoammeter. In all measurements, the upper electrode was connected to the positive side of the current source. The measurements were carried out at room temperature and pressure  $p = 10$  mbar. Before measurements, the samples were annealed at a temperature of  $T = 400$  K in a vacuum for 1.5 h to stabilize their electrical properties.

### 2.6. EPR

Electron paramagnetic resonance (EPR) spectra were recorded with an ELEXSYS-E500 (Bruker, Germany) spectrometer (X-band, sensitivity up to  $10^{10}$  spin/G). The samples were illuminated directly in the spectrometer cavity in the range of 350–900 nm. A mercury lamp was used as the light source. The illumination intensity was of ca.  $40 \text{ mW} \cdot \text{cm}^{-2}$ .

## 3. Results

The morphology of the obtained samples was studied by scanning microscopy. Figure 2 shows SEM images of the resulting nanostructures. The initial TiO<sub>2</sub>-NT arrays have a developed surface with a large number of highly ordered symmetrical pores (Figure 2a,b). The pore diameter distribution is normal. The average pore diameter in the area of  $2.6 \times 1.7 \mu\text{m}$  is about 63 nm. The distance between the pores is about 37 nm. Pores occupy 25% of the surface area of the sample. The height of the nanotube array without hydrothermal treatment is about 6.3  $\mu\text{m}$ . After three hours of hydrothermal treatment or surface modification, a large number of crystals of various shapes and sizes formed on the surface of the TiO<sub>2</sub>-NT. Crystals do not have a specific shape or cut of the crystal lattice. This may be due to the lack of anisotropic growth due to the low alkali concentration in the solution. The pores on the surface are almost completely closed by densely located crystals. The crystal size has an average value of about 217 nm. A cross-section of the sample shows that the crystals are located inside the symmetrical pore channels, which indicates that the reaction is occurring not only on the surface of the sample but also in the volume of the pores. The height of the nanostructured layer after 3 h of treatment is about 6.2  $\mu\text{m}$ . Subsequently, with increasing synthesis time, an increase in the size of the crystals to 230 and 320 nm on the surface of the sample is observed for the samples undergoing synthesis for 6 and 9 h, respectively. This can be explained by the “merging” of individual crystals together during a hydrothermal reaction. The height of the nanostructure decreases with increasing synthesis time. After 6 and 9 h of synthesis, the height was about 5.8 and 5.6  $\mu\text{m}$ . The decrease in height may be associated with the gradual dissolution of the titania and its transition into BaTiO<sub>3</sub> crystals. The sections of the samples show that, with increasing synthesis time, overgrowth of the pore channels is observed. Thus, the symmetry of pores in the samples is broken, and the pores between the BaTiO<sub>3</sub> nanoparticles are arranged randomly.

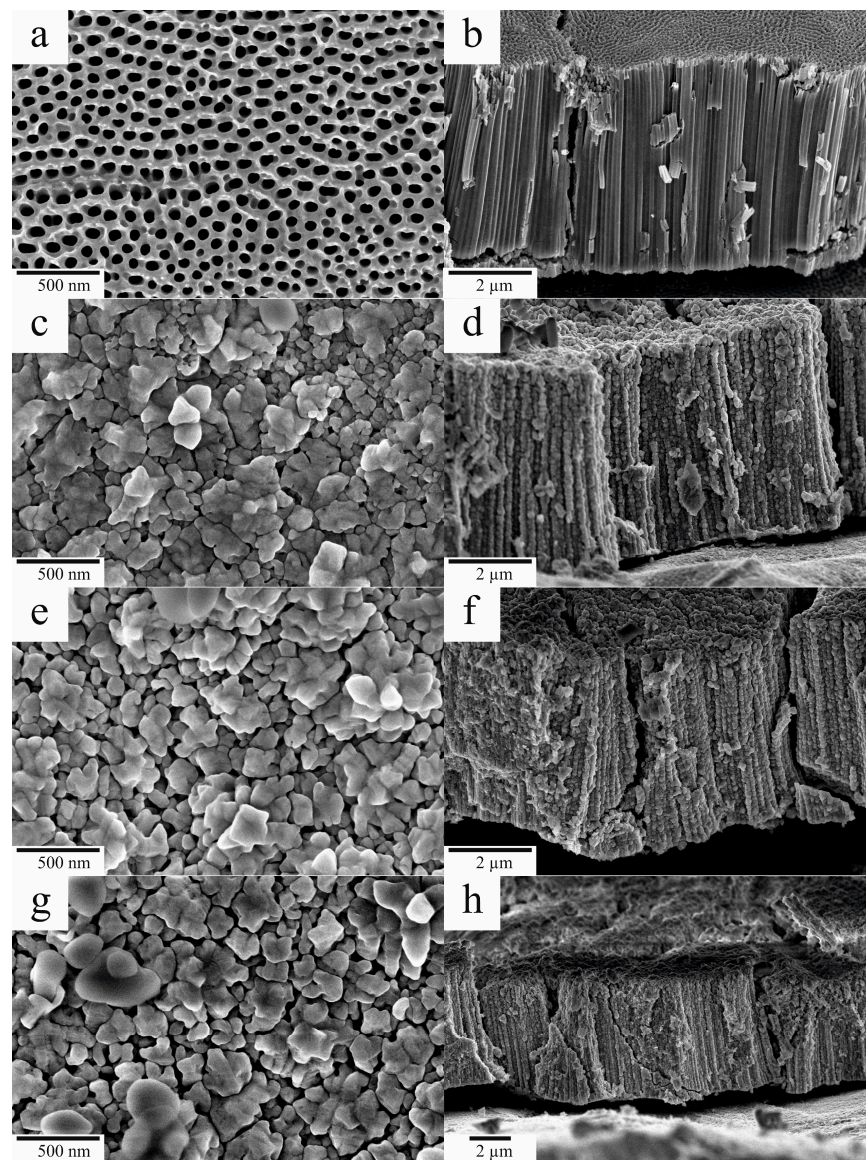


**Figure 2.** SEM images of the obtained samples: (a,b) arrays of symmetrical  $\text{TiO}_2$ -NT, (c,d) 3 h of hydrothermal treatment of  $\text{TiO}_2$ -NT arrays, (e,f) 6 h of hydrothermal treatment of  $\text{TiO}_2$ -NT arrays, (g,h) 9 h.

The chemical composition of the obtained samples was studied by energy-dispersive X-ray spectroscopy; the results are presented in Table 1.

**Table 1.** Results of chemical analysis of the obtained samples.

	0 h	3 h	6 h	9 h
C. at. %	6.3	15.6	14.6	14.0
N. at. %	2.1	6.7	7.8	6.9
O. at. %	61	46.6	45.6	44.1
F. at. %	0.7	0.8	0.8	0.7
Ba. at. %	0.0	19.1	19.6	20.7
Ti. at. %	29.8	11.1	11.6	13.5

The chemical analysis results indicate that the hydrothermal treatment of the symmetrical TiO<sub>2</sub> nanotube arrays leads to the incorporation of Ba into the material composition. Additionally, the carbon content in the material increases significantly, from 6.3 at.% to approximately 15.0 at.%. Notably, the amount of Ba in the material is consistently maintained at a level close to 20.0 at.%, regardless of the duration of the hydrothermal treatment. These findings suggest that the hydrothermal treatment has a significant impact on the material composition, particularly in terms of the incorporation of Ba and the increase in carbon content.

Figure 3 shows the obtained diffraction patterns from the treated samples and the untreated TiO<sub>2</sub>-NT sample.

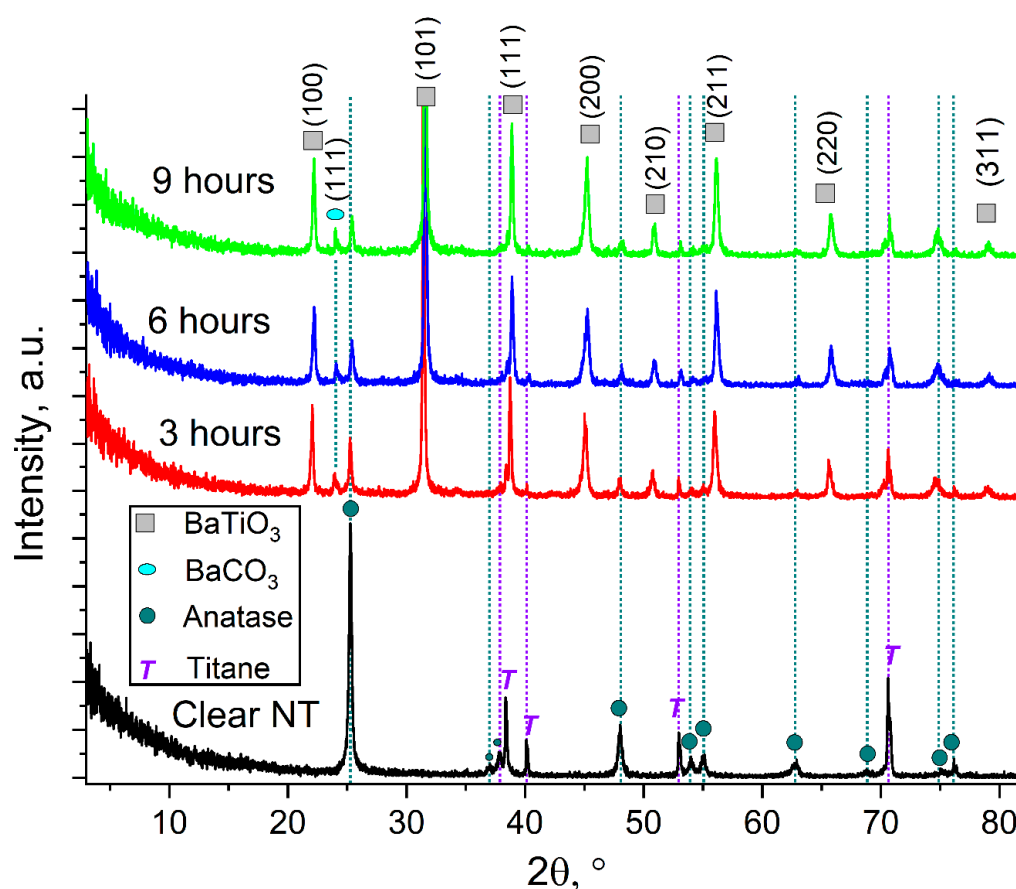


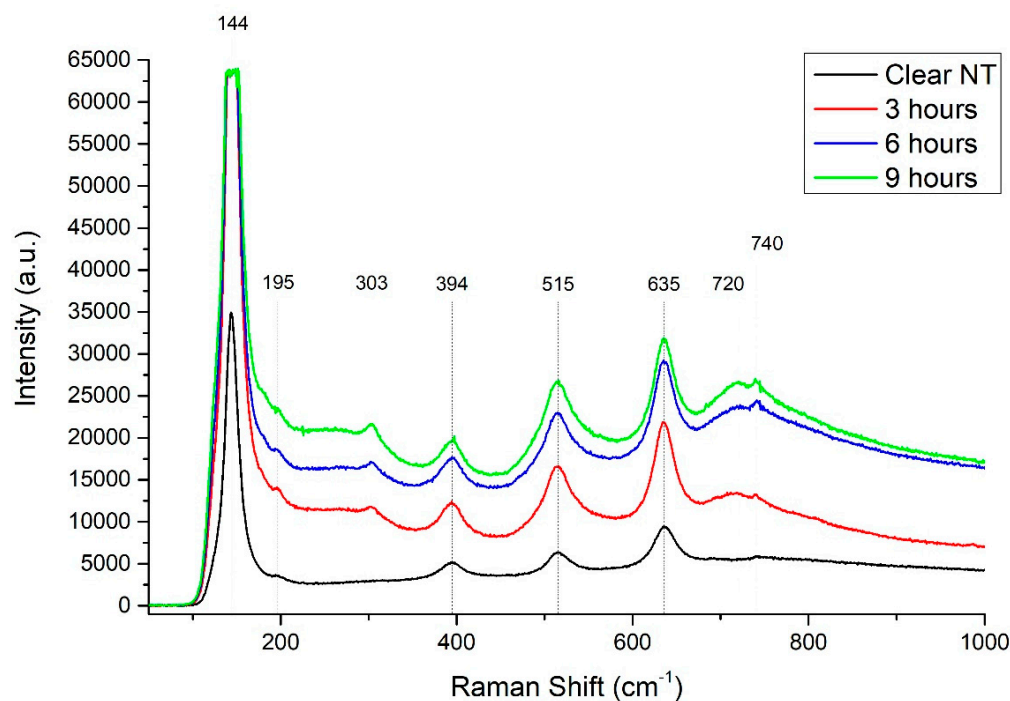
**Figure 3.** X-ray diffraction patterns of TiO<sub>2</sub>-NT with BaTiO<sub>3</sub> obtained by the hydrothermal synthesis during for 3, 6 and 9 h, as well as an untreated TiO<sub>2</sub>-NT sample.

It can be seen from Figure 3 that the diffraction peaks corresponding to TiO<sub>2</sub> (anatase) and titanium substrate (JCPDS-ICDD: 21-1272 and JCPDS-ICDD: 44-1294, respectively) are weakened in the treated samples [12]. In this case, after processing, diffraction peaks appear corresponding to the cubic phase of BaTiO<sub>3</sub> (JCP2.2CAa:31-0174) [24]. The peak corresponding to BaCO<sub>3</sub> (JCPDS No.71-2394) [25], which is a by-product of the hydrothermal reaction, was detected [26]. The source of carbon for the reaction is the inner wall of the nanotube containing carbon dangling bonds [27]. Table 2 presents the viewing angles of the diffraction maxima, their corresponding phase and the orientation of the diffracting planes. No dependence of the intensity, width and shift of the peaks on the treatment time was identified.

**Table 2.** The angles of detected diffraction maxima, their corresponding phases and the orientations of the diffracting planes.

BaTiO <sub>3</sub> (Cubic)		TiO <sub>2</sub> (Anatase)		Ti (Foil)	
2 $\theta$ , °	hkl	2 $\theta$ , °	hkl	2 $\theta$ , °	hkl
22.2	(100)	25.4	(101)	38.4	(002)
31.6	(101)	37.3	(103)	40.3	(101)
38.8	(111)	37.8	(004)	53.3	(102)
45.1	(200)	47.8	(200)	70.5	(103)
50.7	(210)	53.9	(105)	76.5	(112)
56.3	(211)	55.1	(211)		
65.7	(220)	62.3	(204)		BaCO <sub>3</sub>
79.0	(311)	68.6	(116)	24.0	(111)

Raman spectra of titania nanotube samples modified with barium are presented in Figure 4. Let us discuss these results.

**Figure 4.** Raman spectra of TiO<sub>2</sub>-NT samples modified with BaTiO<sub>3</sub>, with different modification times.

According to the reported data [28–30], the TiO<sub>2</sub> anatase phase predominantly exhibits a characteristic line of six main modes, which include A<sub>1g</sub> (519 cm<sup>-1</sup>), B<sub>1g</sub> (399 cm<sup>-1</sup> and 519 cm<sup>-1</sup>) and E<sub>g</sub> (144 cm<sup>-1</sup>, 197 cm<sup>-1</sup> and 639 cm<sup>-1</sup>). At the same time, the spectra of an unmodified sample of TiO<sub>2</sub>-NT arrays showed the presence of peaks of active modes at 144 cm<sup>-1</sup>, 195 cm<sup>-1</sup>, 394 cm<sup>-1</sup>, 515 cm<sup>-1</sup> and 635 cm<sup>-1</sup>, which directly confirms the presence of a pure anatase phase and the absence of other phase peaks rutile (Figure 4). In this study, the assignment of the vibrational bands described below to specific vibrational modes of barium titanate was made based on previous Raman studies of single crystals [31–33], bulk [34,35], thin film [36] and nanocrystalline BaTiO<sub>3</sub> [37,38].

Barium titanate is characterized by three E(TO) modes with frequencies around 186, 280 and 516 cm<sup>-1</sup>. The 186 cm<sup>-1</sup> and 516 cm<sup>-1</sup> modes come from the F<sub>1u</sub> cubic phase modes, and the 303 cm<sup>-1</sup> mode comes from the splitting of the F<sub>2u</sub> cubic mode. The

140, 303, 640  $\text{cm}^{-1}$  and wider 720  $\text{cm}^{-1}$  modes constitute the E(LO) modes. The mode at 280  $\text{cm}^{-1}$  belongs to A1(TO) [39]. Meanwhile, according to the work of Boulos and his colleagues [40], the bands located at 272 and 183  $\text{cm}^{-1}$  are the strongest evidence of the presence of cubic BaTiO<sub>3</sub>. Xiao and co-workers noted [41] that the peak located at 306  $\text{cm}^{-1}$  is the characteristic peak of the tetragonal form of BaTiO<sub>3</sub> [42,43]. At the same time, according to [44–46], the peaks at 281  $\text{cm}^{-1}$ , 305  $\text{cm}^{-1}$ , 514  $\text{cm}^{-1}$  and 720  $\text{cm}^{-1}$  indicate the crystalline cubic phase. The broad peak located near 800  $\text{cm}^{-1}$  in the Raman spectrum is further evidence of the existence of cubic BaTiO<sub>3</sub> [40,43]. According to the literature, cubic BaTiO<sub>3</sub> exhibits two large bands located at 707  $\text{cm}^{-1}$  and 523  $\text{cm}^{-1}$  with significant intensity [35]. Note that, in article [47], the authors note that the decrease and disappearance of the sharp mode at 308  $\text{cm}^{-1}$  and the damped soft mode at 717  $\text{cm}^{-1}$  indicate a cubic phase; we can conclude that these modes belong to the tetragonal system. It is also emphasized in [42] that a decrease in the intensity of the peak at 303  $\text{cm}^{-1}$  may indicate a change in the structure of BaTiO<sub>3</sub> from an asymmetric ferroelectric tetragonal to a more symmetrical (non-ferroelectric) cubic.

In the spectra of samples of TiO<sub>2</sub>-NT arrays modified with Ba, one can see pronounced peaks at 303  $\text{cm}^{-1}$  and 720  $\text{cm}^{-1}$  (Figure 4). The peak corresponding to 303  $\text{cm}^{-1}$  may be due to vibrations in the TiO<sub>6</sub> group or vibrations arising from the displacement of the oxygen atom [44]. In the Raman spectrum of the samples after modification, the described peaks have greater intensity. This may be due to several reasons: the effect of grain size [48,49], blue shift (blue shift means that the frequency or wave number of phonons interacting with the incident photon has increased, and red shift means that it has decreased); softening: (heating, stretching, impurities) red shift; quenching: (cooling, pressure, crystallization) blue shift; oxygen stoichiometry [50,51]; barium substitution in the TiO<sub>2</sub> lattice [52], as well as the phase transition from the cubic phase to the tetragonal phase, depending on the increase in modification time.

It can be concluded that the obtained samples contain both cubic and tetragonal modifications. Due to the fact that the intensity and severity of the peaks increase with the time of hydrothermal treatment, it can be assumed that with the time of the treatment, the proportion of the asymmetric ferroelectric tetragonal phase becomes larger.

The optical properties were studied using the diffuse reflection method. An example of diffuse reflectance spectra in the UV region can be seen in Figure 5.

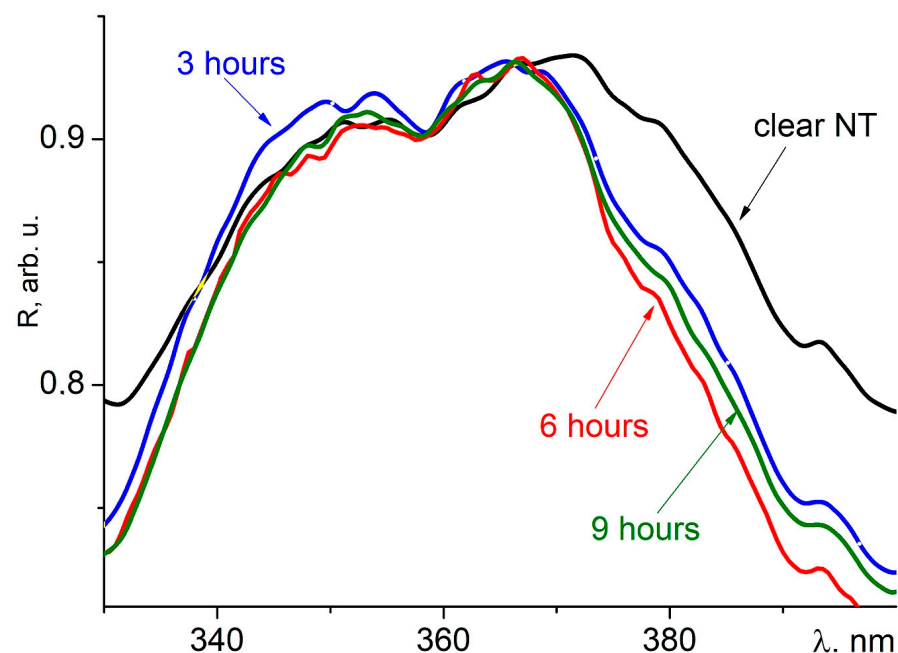


**Figure 5.** Normalized diffuse reflectance spectra of initial TiO<sub>2</sub>-NT arrays and the samples after hydrothermal treatment for 3, 6 and 9 h.

These optical data allow the calculation of absorption and hence the optical band gap for the material. Note that the optical band gap value can be lowered when the defect concentration in the material grows [53]. Using the Kubelka–Munk theory, the values of the optical band gap ( $E_g$ ) were obtained from the diffuse reflectance spectra. To determine the band gap in the case of direct interband transitions, experimental data are presented in the form of the dependence:  $(\alpha h\nu)^2 = A^2(h\nu - E_g)$ . Due to the size effect, the structure of the crystal lattice of nanosized semiconductors changes somewhat, which can lead to an increase in the probability of direct interband transitions [54]. Figure 6 shows a graphical method for obtaining bandgap values using the Kubelka–Munk method. The accuracy of  $E_g$  determination was  $\pm 0.02$  eV. Table 3 presents the values of the obtained parameters.

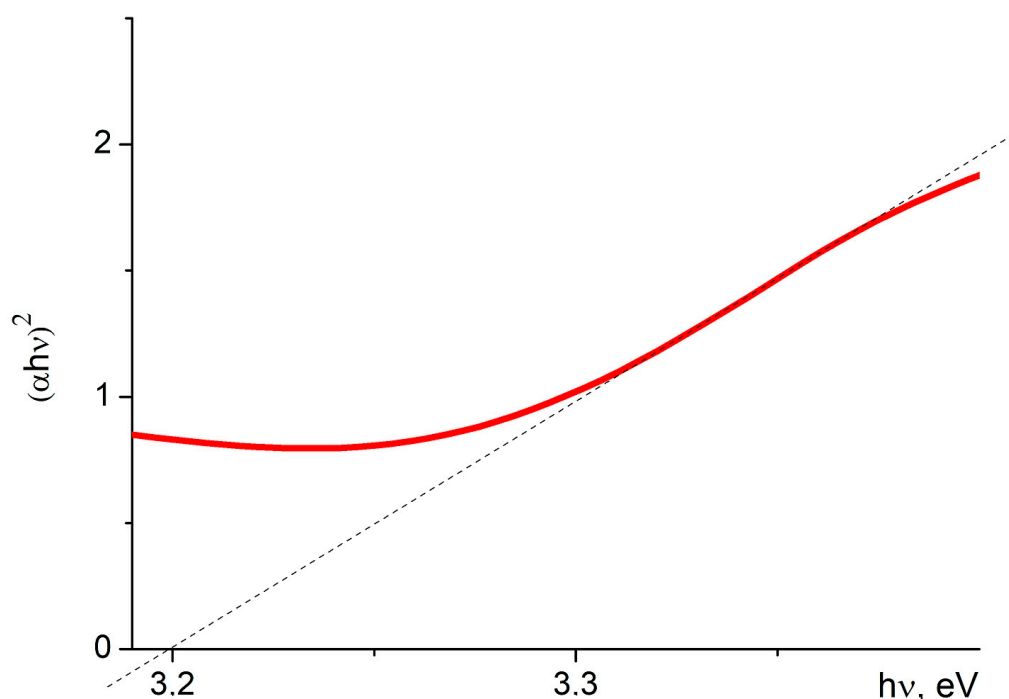


**Figure 6.** An example of determining the optical band gap using the Kubelka–Munk method.

**Table 3.** Optical band gap values for the  $\text{TiO}_2$ -NT and  $\text{TiO}_2$ -NT with  $\text{BaTiO}_3$  (after hydrothermal treatment for 3, 6 and 9 h).

Samples	$E_g$ , eV
Pure $\text{TiO}_2$ -NT	3.20
Processed within 3 h	3.37
Processed within 6 h	3.37
Processed within 9 h	3.31

From the data obtained, we can conclude that the decoration of nanotubes leads to an increase in the optical band gap. Most likely, the increase in  $E_g$  for our samples after hydrothermal treatment indicates the incorporation of barium into the titania lattice. For comparison, we present the literature data for pure barium titanate. For example, the band gap for particles of 6.7 nm in size was measured to be 3.47 eV, which was approximately 0.25 eV larger than that of the  $\text{BaTiO}_3$  bulk [55]. The authors of [56] have found  $E_g = 3.6$  eV for the Langmuir ferroelectric films of  $\text{BaTiO}_3$  with  $\sim 20$  nm grain size. The optical band gap value may be slightly decreased after 9 h of treatment due to the growth of concentration of defects, which creates states near the bottom of the conduction band.

Diffuse reflectance spectra make it possible to determine the difference in the absorption capacity of the samples being studied. Figure 7 shows the spectra of the difference in absorption coefficients of the treated samples relative to the initial.

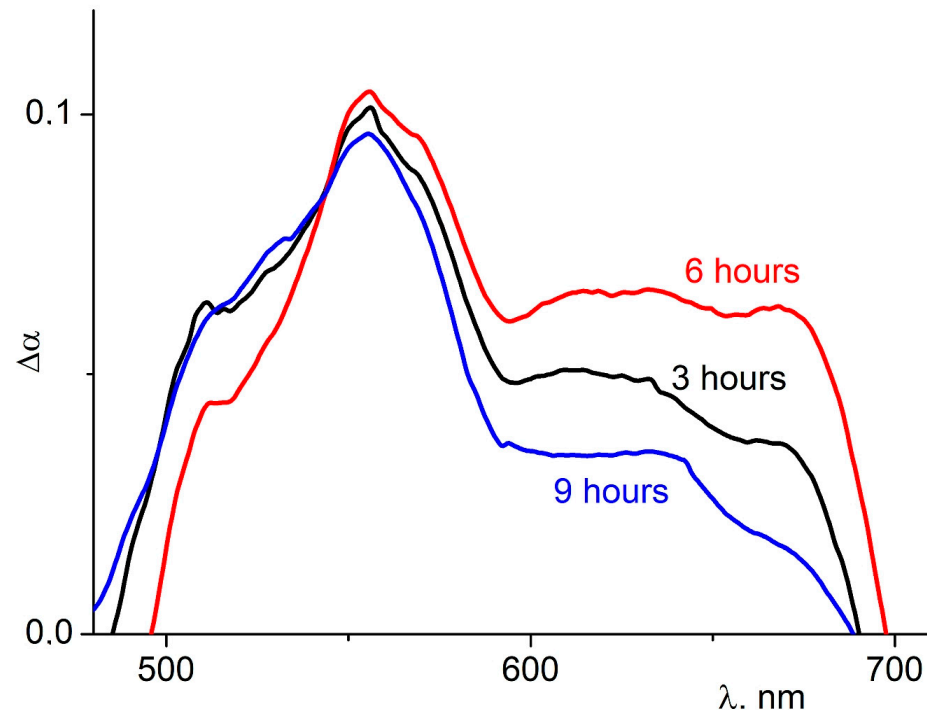


**Figure 7.** Difference in visible light absorption spectra for  $\text{TiO}_2$ -NT with  $\text{BaTiO}_3$  samples compared to the initial sample.

It can be seen from Figure 7 that the absorption coefficient of the visible light for all the processed samples is higher than for the initial samples. It can also be noted that the sample treated for 6 h showed a greater absorption value in the long-wavelength region of the spectrum than other samples.

Let us move on to a discussion of the electrical properties of the samples. Figure 8 shows the current–voltage characteristics of all samples. It can be noted that the current–voltage characteristic of the initial sample (Figure 8a) is nonlinear and symmetrical. This sample is a  $\text{Ti}/\text{TiO}_2/\text{Ti}$  structure. The nonlinearity of the current–voltage characteristic may be associated with the formation of a Schottky barrier at the  $\text{Ti}/\text{TiO}_2$  contact. The symmetry of the obtained dependence indicates that a barrier is formed on both the lower and upper electrodes.

Barium titanate changes the electrical characteristics of the nanotube array to asymmetrical. For samples treated with  $\text{BaTiO}_3$  (Figure 8b–d), the following trend is observed: the current–voltage characteristic becomes asymmetrical, and the asymmetry increases with the treatment time. The highly asymmetrical current–voltage characteristic of the sample processed for 9 h corresponds in appearance to a semiconductor diode. The current strength in the forward direction is significantly higher than the current strength in the reverse direction at the same voltage modulus. The rectification coefficient, which is calculated as the ratio of currents in the forward and reverse directions, for this sample, is  $k = 24$  at a voltage of  $U = 5$  V.

As was previously shown using scanning electron microscopy, sample processing leads to the formation of a layer of  $\text{BaTiO}_3$  particles on the surface of  $\text{TiO}_2$  nanotubes. This leads to the fact that the current–voltage characteristics are measured on an asymmetrical  $\text{Ti}/\text{BaTiO}_3/\text{TiO}_2$ -NT/ $\text{Ti}$  structure (Figure 9).

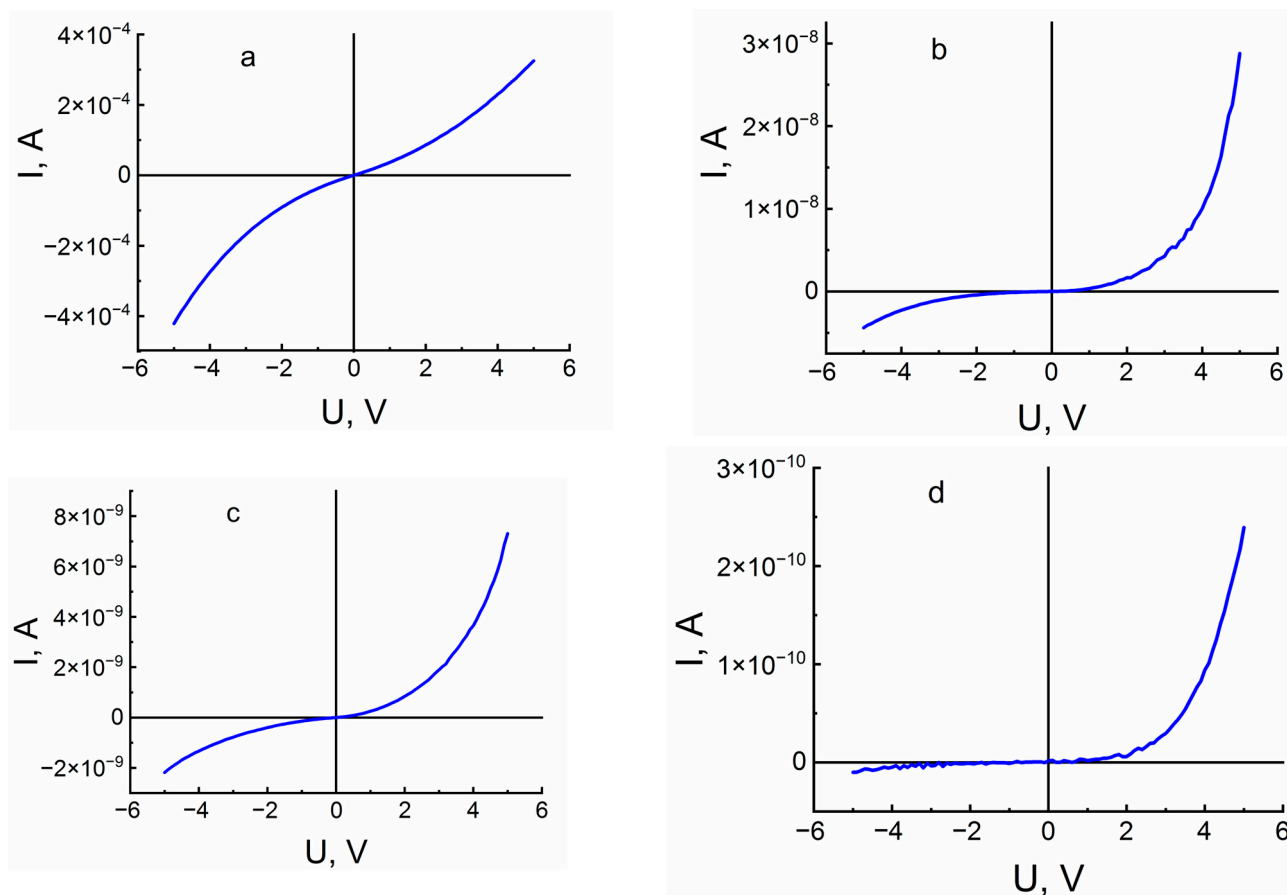


**Figure 8.** Current–voltage characteristics of the original  $\text{TiO}_2$  nanotube sample (a) and samples modified with  $\text{BaTiO}_3$  for 3 (b), 6 (c) and 9 h (d).

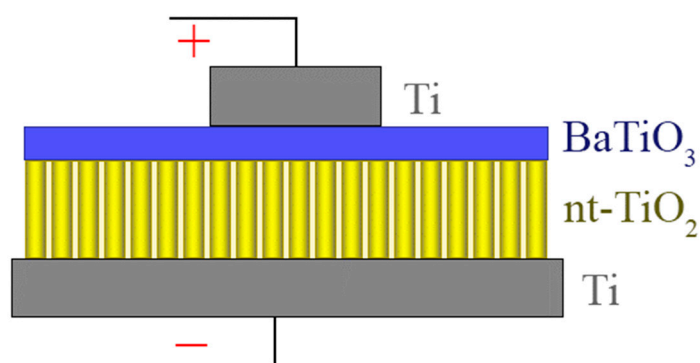


**Figure 9.** Schematic of the  $\text{Ti}/\text{BaTiO}_3/\text{TiO}_2\text{-NT}/\text{Ti}$  structure.

The observed type of current–voltage characteristics for samples treated with barium titanate can be explained by the formation of a  $\text{TiO}_2/\text{BaTiO}_3$  nanoheterojunction. An increase in the thickness of the layer of  $\text{BaTiO}_3$  particles with increasing treatment time leads to an increase in the height of the potential barrier formed at the heterojunction. Thus, measuring the current–voltage characteristics makes it possible to clearly demonstrate the possibility of forming a  $\text{TiO}_2/\text{BaTiO}_3$  nanoheterojunction. The electric field, which always arises near the heterojunction, promotes the separation of the nonequilibrium charge carriers that arise during illumination and increases their lifetime, which in turn ensures better photoactivity of the material. These data are in good agreement with the results of EPR spectroscopy.

The EPR spectra of TiO<sub>2</sub>-NT/BaTiO<sub>3</sub> samples with a modification time of 6 h are shown in Figure 10 as an example. In the magnetic field range of 2200–3800 G, a broad EPR signal is observed, which is a superposition of the EPR lines from defects: titanium vacancies (V<sub>Ti</sub>) with  $g = 2.004$  and barium vacancies (V<sub>Ba</sub>) with  $g = 1.974$  (Figure 10) [57,58]. In the magnetic field range 3800–4100 G there is an EPR signal with  $g = 1.912$ , which is caused by Ti<sup>3+</sup>/V<sub>O</sub> (oxygen vacancies) [57]. When illuminated, the intensity of EPR signals from titanium and barium vacancies decreased by more than one and a half times. The intensity of the EPR signal from oxygen vacancies increases under illumination.

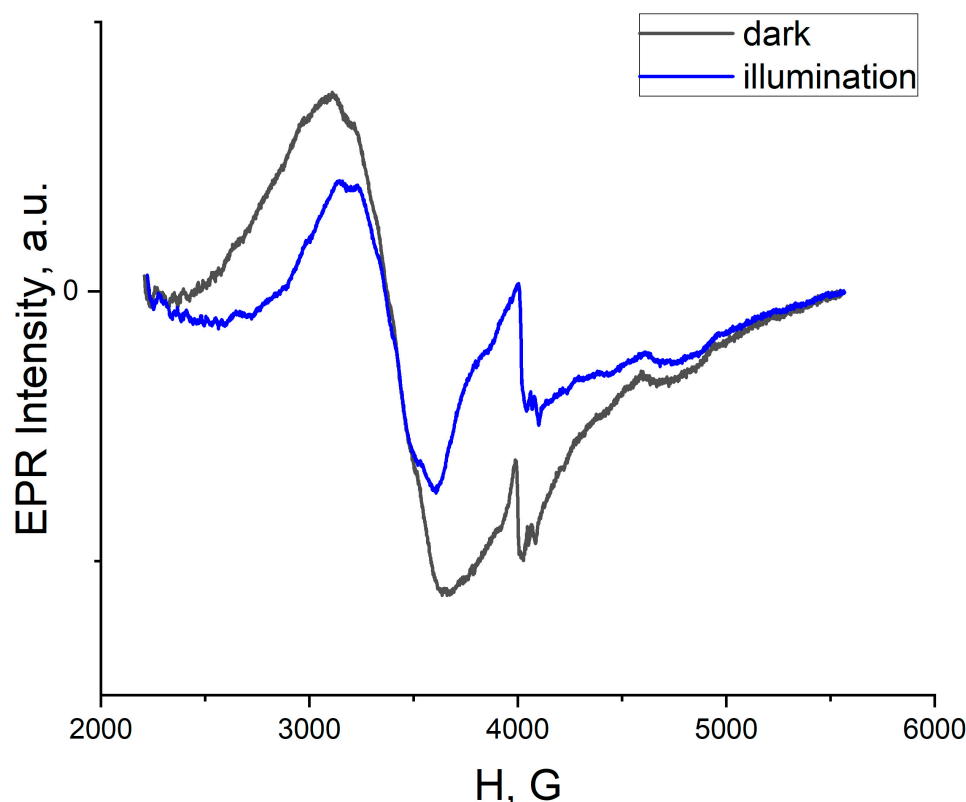


**Figure 10.** EPR spectra of TiO<sub>2</sub>-NT/BaTiO<sub>3</sub> with a modification time of 6 h in the dark and under illumination.

After turning off the illumination, the intensity of the EPR signals from metal vacancies returned to its initial state over a long period of time—approximately 24 h. The decrease in the intensity of EPR signals from defects under illumination can be explained by their recharging. Photoexcited electrons and holes are probably separated between the TiO<sub>2</sub> and BaTiO<sub>3</sub> forming the nanoheterojunction (Figure 11). Photoexcited holes are captured by titanium and barium vacancies in barium titanate, so the vacancies become non-paramagnetic (lose an electron). Therefore, the intensity of the EPR signal from titanium and barium vacancies decreases upon illumination (Figure 10). Non-paramagnetic oxygen vacancies (not containing an electron) in titanium oxide capture photoexcited electrons, so the intensity of the EPR signal from oxygen vacancies increases upon illumination (Figure 10). After turning off the illumination, the intensity of the EPR signals from oxygen vacancies returned to its original state very slowly—during 24 h (Figure 12). Unmodified samples of TiO<sub>2</sub>-NT are also shown in Figure 12 (inset) for comparison. As can be seen from Figure 12 (inset), the relaxation of the EPR signal intensity in the titania occurs quite quickly (within two hours) due to the recombination of photoexcited electrons and holes in the titania.

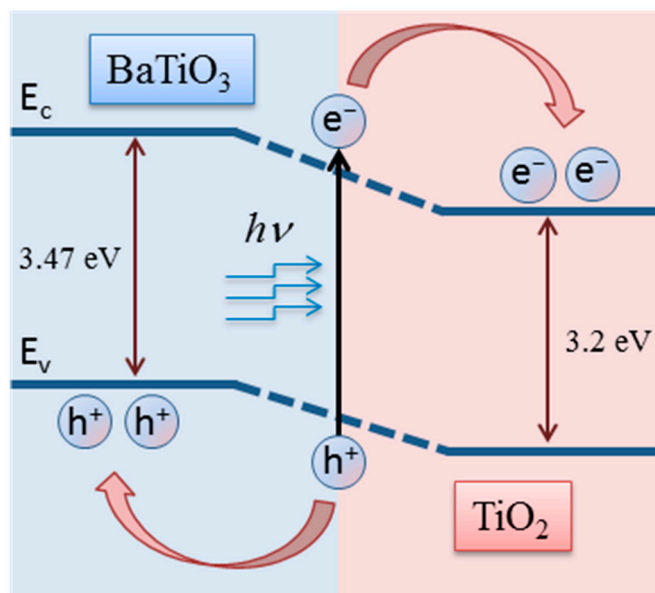


**Figure 11.** A schematic representation of the process of separation of photoinduced charge carriers arising under illumination. The electric field generated in the heterojunction region due to the diffusion of charge carriers leads to the separation of nonequilibrium electrons and holes. As a result, electrons go into titania and holes go into barium titanate.

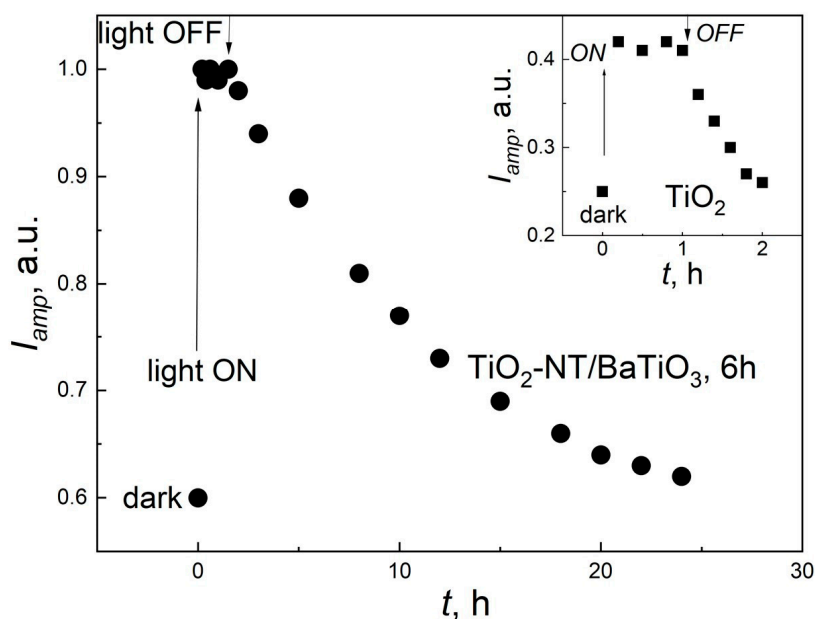


**Figure 12.** Relaxation kinetics of EPR signal intensity after turning off the illumination (OFF) for samples of TiO<sub>2</sub>-NT/BaTiO<sub>3</sub> with a modification time of 6 h and of TiO<sub>2</sub>-NT (inset).

Note that for nanoheterostructures, due to the asymmetric separation of photoexcited electrons and holes between different semiconductors (TiO<sub>2</sub>-NT and BaTiO<sub>3</sub>), their recombination is suppressed. This explains why the intensity of the EPR signal from defects relaxes to the initial state for such a long time after turning off the illumination. Thus, photoexcited holes and electrons are captured by titanium, barium and oxygen vacancies, respectively, and charge accumulation occurs in the TiO<sub>2</sub>-NT/BaTiO<sub>3</sub> nanoheterostructures.

#### 4. Conclusions

The symmetrical TiO<sub>2</sub>-NT arrays were prepared using the electrochemical method. The modification of the obtained symmetrical TiO<sub>2</sub>-NT arrays was carried out by hydrother-

mal treatment in an aqueous solution of barium hydroxide. The structure and chemical composition of the obtained samples were studied, and it was found that the samples have a crystalline structure. According to energy-dispersive X-ray spectroscopy data, the samples contain carbon, nitrogen, barium and traces of fluorine. Using diffuse reflectance spectroscopy, the optical band gap was determined, which was 3.2 eV and 3.37 eV for the TiO<sub>2</sub>-NT and TiO<sub>2</sub>-NT/BaTiO<sub>3</sub> samples, respectively. The current–voltage characteristics of TiO<sub>2</sub>-NT modified with barium titanate become asymmetrical and can be explained by the formation of the TiO<sub>2</sub>/BaTiO<sub>3</sub> nanoheterojunction. Thus, modification of symmetrical TiO<sub>2</sub>-NT with barium titanate nanoparticles changes the structure and electrical characteristics of the nanotube array to asymmetrical. Paramagnetic defects such as titanium, barium and oxygen vacancies are detected in TiO<sub>2</sub>-NT/BaTiO<sub>3</sub> using EPR spectroscopy. It was discovered for the first time that, under the illumination of the TiO<sub>2</sub> nanotubes modified with BaTiO<sub>3</sub>, the photoexcited electrons and holes are asymmetrically separated between TiO<sub>2</sub>-NT and BaTiO<sub>3</sub>. This process leads to the effective charge accumulation on defects in the TiO<sub>2</sub>-NT/BaTiO<sub>3</sub> nanoheterostructures. The obtained results are completely new and show good application prospects of the TiO<sub>2</sub>-NT/BaTiO<sub>3</sub> nanocomposites with an asymmetrical structure in the field of photocatalytic and photovoltaic applications.

**Author Contributions:** Conceptualization, E.K. (Elizaveta Konstantinova) and T.S.; methodology, M.M.; software, D.B. and E.K. (Ekaterina Kytina); validation, V.Z. and E.K. (Elizaveta Konstantinova); formal analysis, T.S. and E.K. (Ekaterina Kytina); investigation, T.S., D.B., L.V., D.D., D.K., E.K. (Ekaterina Kytina), M.M., V.Z., A.T. and E.K. (Elizaveta Konstantinova); data curation, E.K. (Elizaveta Konstantinova); writing—original draft preparation, T.S., V.Z., M.M., D.K. and E.K. (Elizaveta Konstantinova); writing—review and editing, E.K. (Elizaveta Konstantinova), T.S., V.Z., D.D. and E.K. (Ekaterina Kytina); visualization, L.V. and A.T.; supervision, E.K. (Elizaveta Konstantinova). All authors have read and agreed to the published version of the manuscript.

**Funding:** Synthesis of samples, optical, electrophysical measurement and EPR spectroscopy study was supported by a grant from the Russian Science Foundation No 21-19-00494, <https://rscf.ru/en/project/21-19-00494/> (accessed on 1 October 2023). The Raman spectroscopy and XRD measurements was supported by State Assignment № FSMR-2023-0003.

**Data Availability Statement:** The data presented in this study are available on request.

**Acknowledgments:** EPR measurements were performed using the facilities of the Collective Use Center at the Physics Department of M.V. Lomonosov Moscow State University (<http://ckp-nano.msu.ru/structure/5> (accessed on 1 October 2023)).

**Conflicts of Interest:** The authors declare no conflict of interest.

## References

1. Chen, S.; Zhou, Y.; Luo, H.; Tang, L.; Guo, R.; Zhang, D. Core-shell TiO<sub>2</sub>@HfO<sub>2</sub> nanowire arrays with designable shell thicknesses for improved permittivity and energy density in polymer nanocomposites. *Compos. Part A Appl. Sci. Manuf.* **2020**, *137*, 106012. [[CrossRef](#)]
2. Choi, J.O.; Kim, T.Y.; Park, S.M.; Seol, W.; Joh, H.; Anoop, G.; Jo, J.Y. Co:BaTiO<sub>3</sub>/Sn:BaTiO<sub>3</sub> Heterostructure Thin-Film Capacitors with Ultrahigh Energy Density and Breakdown Strength. *Adv. Electron. Mater.* **2023**, *9*, 2201141. [[CrossRef](#)]
3. Liu, Q.; Li, Z.; Li, J.; Zhan, F.; Zhai, D.; Sun, Q.; Xiao, Z.; Luo, H.; Zhang, D. Three Dimensional BaTiO<sub>3</sub> Piezoelectric Ceramics Coated with TiO<sub>2</sub> Nanoarray for High Performance of Piezo-Photoelectric Catalysis. *Nano Energy* **2022**, *98*, 107267. [[CrossRef](#)]
4. Long, X.; Tan, H.; Sánchez, F.; Fina, I.; Fontcuberta, J. Disentangling Electronic and Thermal Contributions to Light-Induced Resistance Switching in BaTiO<sub>3</sub> Ferroelectric Tunnel Junction. *J. Appl. Phys.* **2022**, *132*, 214103. [[CrossRef](#)]
5. Fakhar-e-Alam, M.; Saddique, S.; Hossain, N.; Shahzad, A.; Ullah, I.; Sohail, A.; Khan, M.J.I.; Saadullah, M. Synthesis, Characterization, and Application of BaTiO<sub>3</sub> Nanoparticles for Anti-Cancer Activity. *J. Clust. Sci.* **2023**, *34*, 1745–1755. [[CrossRef](#)]
6. Cho, Y.; Jeong, J.; Choi, M.; Baek, G.; Park, S.; Choi, H.; Ahn, S.; Cha, S.; Kim, T.; Kang, D.-S.; et al. BaTiO<sub>3</sub>@PVDF-TrFE Nanocomposites with Efficient Orientation Prepared via Phase Separation Nano-Coating Method for Piezoelectric Performance Improvement and Application to 3D-PENG. *Chem. Eng. J.* **2022**, *427*, 131030. [[CrossRef](#)]
7. Shihab, N.K.; Acharyya, J.N.; Rasi, U.P.M.; Gangineni, R.B.; Lakshmi, P.A.; Prakash, G.V.; Rao, D.N. Nonlinear Optical Absorption Switching Behavior of BaTiO<sub>3</sub> in Asymmetric Microcavity. *Opt. Mater.* **2020**, *101*, 109777. [[CrossRef](#)]

8. Varghese, O.K.; Grimes, C.A. Appropriate Strategies for Determining the Photoconversion Efficiency of Water Photoelectrolysis Cells: A Review with Examples Using Titania Nanotube Array Photoanodes. *Sol. Energy Mater. Sol. Cells* **2008**, *92*, 374–384. [[CrossRef](#)]
9. Navidpour, A.H.; Abbasi, S.; Li, D.; Mojiri, A.; Zhou, J.L. Investigation of advanced oxidation process in the presence of TiO<sub>2</sub> semiconductor as photocatalyst: Property, principle, kinetic analysis, and photocatalytic activity. *Catalysts* **2023**, *13*, 232. [[CrossRef](#)]
10. Patel, M.; Hemanth, N.R.; Gosai, J.; Mohili, R.; Solanki, A.; Roy, M.; Chaudhari, N.K. MXenes: Promising 2D memristor materials for neuromorphic computing components. *Trends Chem.* **2022**, *4*, 835–849. [[CrossRef](#)]
11. Park, S.; Spetzler, B.; Ivanov, T.; Ziegler, M. Multilayer redox-based HfOx/Al<sub>2</sub>O<sub>3</sub>/TiO<sub>2</sub> memristive structures for neuromorphic computing. *Sci. Rep.* **2022**, *12*, 18266. [[CrossRef](#)] [[PubMed](#)]
12. Savchuk, T.; Gavrilin, I.; Savitskiy, A.; Dronov, A.; Dronova, D.; Pereverzeva, S.; Tarhanov, A.; Maniecki, T.; Gavrilov, S.; Konstantinova, E. Effect of Thermal Treatment of Symmetric TiO<sub>2</sub> Nanotube Arrays in Argon on Photocatalytic CO<sub>2</sub> Conversion. *Symmetry* **2022**, *14*, 2678. [[CrossRef](#)]
13. Roy, P.; Berger, S.; Schmuki, P. TiO<sub>2</sub> nanotubes: Synthesis and applications. *Angew. Chem. Int. Ed.* **2011**, *50*, 2904–2939. [[CrossRef](#)] [[PubMed](#)]
14. Savchuk, T.; Gavrilin, I.; Konstantinova, E.; Dronov, A.; Volkov, R.; Borgardt, N.; Zaitsev, V. Anodic TiO<sub>2</sub> nanotube arrays for photocatalytic CO<sub>2</sub> conversion: Comparative photocatalysis and EPR study. *Nanotechnology* **2021**, *33*, 055706. [[CrossRef](#)] [[PubMed](#)]
15. Opra, D.P.; Sokolov, A.A.; Sinebryukhov, S.L.; Tkachenko, I.A.; Ziatdinov, A.M.; Gnedenkov, S.V. Electronic Structure, Optical and Magnetic Properties of Oxygen-Deficient Gray TiO<sub>2-δ</sub> (B). *Inorganics* **2022**, *10*, 184. [[CrossRef](#)]
16. Kytina, E.V.; Savchuk, T.P.; Gavrilin, I.M.; Konstantinova, E.A. Photoinduced Dynamics of Spin Centers in Carbon-Modified Titanium Dioxide Nanotubes. *Russ. J. Inorg. Chem.* **2023**, *1*, 6. [[CrossRef](#)]
17. Ivanovskaya, M.; Chernyakova, K.; Ovodok, E.; Poznyak, S.K.; Kotsikau, D.; Azarko, I.I. Nature of Paramagnetic Defects in Black Titanium Dioxide Nanotubes. *Mater. Chem. Phys.* **2022**, *278*, 125703. [[CrossRef](#)]
18. Konstantinova, E.; Savchuk, T.; Pinchuk, O.; Kytina, E.; Ivanova, E.; Volkova, L.; Elizarova, E. Photoelectron Properties and Organic Molecules Photodegradation Activity of Titania Nanotubes with Cu<sub>x</sub>O Nanoparticles Heat Treated in Air and Argon. *Molecules* **2022**, *27*, 8080. [[CrossRef](#)]
19. Li, Z.; Wang, S.; Wu, J.; Zhou, W. Recent progress in defective TiO<sub>2</sub> photocatalysts for energy and environmental applications. *Renew. Sustain. Energy Rev.* **2022**, *156*, 111980. [[CrossRef](#)]
20. Barrocas, B.T.; Ambrožová, N.; Kočí, K. Photocatalytic reduction of carbon dioxide on TiO<sub>2</sub> heterojunction photocatalysts—A review. *Materials* **2022**, *15*, 967. [[CrossRef](#)]
21. Lettieri, S.; Pavone, M.; Fioravanti, A.; Santamaria Amato, L.; Maddalena, P. Charge carrier processes and optical properties in TiO<sub>2</sub> and TiO<sub>2</sub>-based heterojunction photocatalysts: A review. *Materials* **2021**, *14*, 1645. [[CrossRef](#)] [[PubMed](#)]
22. Rawat, J.; Rawat, S.; Juyal, A.; Sharma, H.; Dwivedi, C. Enhancing electrochemical properties of TiO<sub>2</sub> nanotube by incorporation of CdSe quantum dots. *J. Nanopart. Res.* **2023**, *25*, 82. [[CrossRef](#)]
23. Wang, S.; Yu, C.; Chen, X.; Zhang, K.; Gao, H.; Yu, X.; Zhang, J. Synthesis and characterization of BaTiO<sub>3</sub>/TiO<sub>2</sub> heterojunction photocatalyst for novel application in photocatalytic degradation of TBBPA under simulated sunlight irradiation. *ChemistrySelect* **2022**, *7*, e202202764. [[CrossRef](#)]
24. Shcherbina, N.A.; Kazakov, I.V.; Timoshkin, A.Y. Synthesis and Characterization of Barium Amidoborane. *Russ. J. Gen. Chem.* **2017**, *87*, 2875–2877. [[CrossRef](#)]
25. Hu, X.; Lu, P.; He, Y.; Wang, C.; Chen, J.; Fu, M. Anionic/cationic synergistic action of insulator BaCO<sub>3</sub> enhanced the photocatalytic activities of graphitic carbon nitride. *Appl. Surf. Sci.* **2020**, *528*, 146924. [[CrossRef](#)]
26. Vijayalakshmi, R.; Rajendran, V. Synthesis of BaTiO<sub>3</sub> and Evaluation of Optical Properties. *Azo J. Mater. Online* **2010**, *6*. [[CrossRef](#)]
27. Gavrilin, I.; Dronov, A.; Volkov, R.; Savchuk, T.; Dronova, D.; Borgardt, N.; Gromov, D. Differences in the local structure and composition of anodic TiO<sub>2</sub> nanotubes annealed in vacuum and air. *Appl. Surf. Sci.* **2020**, *516*, 146120. [[CrossRef](#)]
28. Yanagisawa, K.; Ovenstone, J. Crystallization of Anatase from Amorphous Titania Using the Hydrothermal Technique: Effects of Starting Material and Temperature. *J. Phys. Chem. B* **1999**, *103*, 7781–7787. [[CrossRef](#)]
29. Su, W.; Zhang, J.; Feng, Z.; Chen, T.; Ying, P.; Li, C. Surface Phases of TiO<sub>2</sub> Nanoparticles Studied by UV Raman Spectroscopy and FT-IR Spectroscopy. *J. Phys. Chem. C* **2008**, *112*, 7710–7716. [[CrossRef](#)]
30. Appadurai, T.; Subramaniam, C.; Kuppusamy, R.; Karazhanov, S.; Subramanian, B. Electrochemical Performance of Nitrogen-Doped TiO<sub>2</sub> Nanotubes as Electrode Material for Supercapacitor and Li-Ion Battery. *Molecules* **2019**, *24*, 2952. [[CrossRef](#)]
31. Dobal, P.S.; Dixit, A.; Katiyar, R.S.; Yu, Z.; Guo, R.; Bhalla, A.S. Micro-Raman Scattering and Dielectric Investigations of Phase Transition Behavior in the BaTiO<sub>3</sub>–BaZrO<sub>3</sub> System. *J. Appl. Phys.* **2001**, *89*, 8085–8091. [[CrossRef](#)]
32. Wada, S.; Suzuki, T.; Osada, M.; Kakihana, M.; Noma, T. Change of Macroscopic and Microscopic Symmetry of Barium Titanate Single Crystal around Curie Temperature. *Jpn. J. Appl. Phys.* **1998**, *37*, 5385. [[CrossRef](#)]
33. Perry, C.H.; Hall, D.B. Temperature Dependence of the Raman Spectrum of BaTiO<sub>3</sub>. *Phys. Rev. Lett.* **1965**, *15*, 700–702. [[CrossRef](#)]
34. Busca, G.; Ramis, G.; Amores, J.M.G.; Escribano, V.S.; Piaggio, P. FT Raman and FTIR Studies of Titanias and Metatitanate Powders. *J. Chem. Soc. Faraday Trans.* **1994**, *90*, 3181. [[CrossRef](#)]
35. Busca, G.; Buscaglia, V.; Leoni, M.; Nanni, P. Solid-State and Surface Spectroscopic Characterization of BaTiO<sub>3</sub> Fine Powders. *Chem. Mater.* **1994**, *6*, 955–961. [[CrossRef](#)]

36. Robins, L.H.; Kaiser, D.L.; Rotter, L.D.; Schenck, P.K.; Stauf, G.T.; Rytz, D. Investigation of the Structure of Barium Titanate Thin Films by Raman Spectroscopy. *J. Appl. Phys.* **1994**, *76*, 7487–7498. [[CrossRef](#)]
37. Smith, M.B.; Page, K.; Siegrist, T.; Redmond, P.L.; Walter, E.C.; Seshadri, R.; Brus, L.E.; Steigerwald, M.L. Crystal Structure and the Paraelectric-to-Ferroelectric Phase Transition of Nanoscale BaTiO<sub>3</sub>. *J. Am. Chem. Soc.* **2008**, *130*, 6955–6963. [[CrossRef](#)]
38. Shiratori, Y.; Pithan, C.; Dornseiffer, J.; Waser, R. Raman Scattering Studies on Nanocrystalline BaTiO<sub>3</sub> Part I—Isolated Particles and Aggregates. *J. Raman Spectrosc.* **2007**, *38*, 1288–1299. [[CrossRef](#)]
39. Yuzyuk, Y.I. Raman Scattering Spectra of Ceramics, Films, and Superlattices of Ferroelectric Perovskites: A Review. *Phys. Solid State* **2012**, *54*, 1026–1059. [[CrossRef](#)]
40. Boulos, M.; Guillemetfritsch, S.; Mathieu, F.; Durand, B.; Lebey, T.; Bley, V. Hydrothermal Synthesis of Nanosized BaTiO<sub>3</sub> Powders and Dielectric Properties of Corresponding Ceramics. *Solid State Ion.* **2005**, *176*, 1301–1309. [[CrossRef](#)]
41. Xiao, C.J.; Chi, Z.H.; Zhang, W.W.; Li, F.Y.; Feng, S.M.; Jin, C.Q.; Wang, X.H.; Deng, X.Y.; Li, L.T. The Phase Transitions and Ferroelectric Behavior of Dense Nanocrystalline BaTiO<sub>3</sub> Ceramics Fabricated by Pressure Assisted Sintering. *J. Phys. Chem. Solids* **2007**, *68*, 311–314. [[CrossRef](#)]
42. Lazarević, Z.; Romčević, N.; Vijatović, M.; Paunović, N.; Romčević, M.; Stojanović, B.; Dohčević-Mitrović, Z. Characterization of Barium Titanate Ceramic Powders by Raman Spectroscopy. *Acta Phys. Pol. A* **2009**, *115*, 808–810. [[CrossRef](#)]
43. Wu, X.; Chen, Z.; Cui, Z. Low Temperature Synthesis of Cubic BaTiO<sub>3</sub> Nanoparticles. In Proceedings of the The 8th Annual IEEE International Conference on Nano/Micro Engineered and Molecular Systems, Suzhou, China, 7–10 April 2013; pp. 399–402.
44. Singh, M.; Yadav, B.C.; Ranjan, A.; Kaur, M.; Gupta, S.K. Synthesis and Characterization of Perovskite Barium Titanate Thin Film and Its Application as LPG Sensor. *Sens. Actuators B Chem.* **2017**, *241*, 1170–1178. [[CrossRef](#)]
45. Yuan, Y.; Zhang, S.R.; Zhou, X.H.; Tang, B.; Li, B. High-Temperature Capacitor Materials Based on Modified BaTiO<sub>3</sub>. *J. Electron. Mater.* **2009**, *38*, 706–710. [[CrossRef](#)]
46. Venkateswaran, U.D.; Naik, V.M.; Naik, R. High-Pressure Raman Studies of Polycrystalline BaTiO<sub>3</sub>. *Phys. Rev B* **1998**, *58*, 14256–14260. [[CrossRef](#)]
47. Madhan, K.; Thiyagarajan, R.; Jagadeeshwaran, C.; Paul Blessington Selvadurai, A.; Pazhanivelu, V.; Aravinth, K.; Yang, W.; Murugaraj, R. Investigations on the Phase Transition of Mn-Doped BaTiO<sub>3</sub> Multifunctional Ferroelectric Ceramics through Raman, Dielectric, and Magnetic Studies. *J. Solgel Sci. Technol.* **2018**, *88*, 584–592. [[CrossRef](#)]
48. Yang, M.; Huang, D.; Hao, P.; Zhang, F.; Hou, X.; Wang, X. Study of the Raman Peak Shift and the Linewidth of Light-Emitting Porous Silicon. *J. Appl. Phys.* **1994**, *75*, 651–653. [[CrossRef](#)]
49. Campbell, I.H.; Fauchet, P.M. The Effects of Microcrystal Size and Shape on the One Phonon Raman Spectra of Crystalline Semiconductors. *Solid State Commun.* **1986**, *58*, 739–741. [[CrossRef](#)]
50. Parker, J.C.; Siegel, R.W. Calibration of the Raman Spectrum to the Oxygen Stoichiometry of Nanophase TiO<sub>2</sub>. *Appl. Phys. Lett.* **1990**, *57*, 943–945. [[CrossRef](#)]
51. Chen, S.; Xiao, Y.; Wang, Y.; Hu, Z.; Zhao, H.; Xie, W. A Facile Approach to Prepare Black TiO<sub>2</sub> with Oxygen Vacancy for Enhancing Photocatalytic Activity. *Nanomaterials* **2018**, *8*, 245. [[CrossRef](#)]
52. Wang, J.; Zhu, W.; Zhang, Y.; Liu, S. An Efficient Two-Step Technique for Nitrogen-Doped Titanium Dioxide Synthesizing: Visible-Light-Induced Photodecomposition of Methylene Blue. *J. Phys. Chem. C* **2007**, *111*, 1010–1014. [[CrossRef](#)]
53. Tang, H.; Prasad, K.; Sanjines, R.; Schmid, P.E.; Levy, F. Electrical and optical properties of TiO<sub>2</sub> anatase thin films. *Appl. Phys.* **1994**, *75*, 2042–2047. [[CrossRef](#)]
54. Byung-Hyun, K.; Mina, P.; Gyubong, K.; Hermansson, K.; Broqvist, P.; Heon-Jin, C.; Kwang-Ryeol, L. Indirect-to-Direct Band Gap Transition of Nanosheets: Effect of Biaxial Strain. *J. Phys. Chem. C* **2018**, *122*, 15297–15303. [[CrossRef](#)]
55. Suzuki, K.; Kijima, K. Optical Band Gap of Barium Titanate Nanoparticles Prepared by RF-Plasma Chemical Vapor Deposition. *Jpn. J. Appl. Phys.* **2005**, *44*, 2081. [[CrossRef](#)]
56. Kuzmenko, A.P.; Chukhaeva, I.V.; Abakumov, P.V. Features of the Formation and Structure of Barium Titanate Langmuir Films. *Tech. Phys.* **2019**, *64*, 1168–1177. [[CrossRef](#)]
57. Brzozowski, E.; Castro, M.S. Grain growth control in Nb-doped BaTiO<sub>3</sub>. *J. Mater. Process. Technol.* **2005**, *168*, 464–470. [[CrossRef](#)]
58. Da-Yong Lu, D.-Y.; Guan, D.-X. Photoluminescence associated with the site occupations of Ho<sup>3+</sup> ions in BaTiO<sub>3</sub>. *Sci. Rep.* **2017**, *7*, 6125. [[CrossRef](#)]

**Disclaimer/Publisher's Note:** The statements, opinions and data contained in all publications are solely those of the individual author(s) and contributor(s) and not of MDPI and/or the editor(s). MDPI and/or the editor(s) disclaim responsibility for any injury to people or property resulting from any ideas, methods, instructions or products referred to in the content.